The Astrophysical Journal, 974:27 (9pp), 2024 October 10 https://doi.org/10.3847/1538-4357/ad702c

High-redshift Halo–Galaxy Connection via Constrained Simulations

Adi Nusser

Department of Physics and the Asher Space Research Institute, Israel Institute of Technology Technion, Haifa 32000, Israel; adi@physics.technion.ac.il

Received 2024 February 29; revised 2024 August 13; accepted 2024 August 13; published 2024 October 3

Abstract

The evolution of halos with masses around $M_{\rm h} \approx 10^{11}\,M_\odot$ and $M_{\rm h} \approx 10^{12}\,M_\odot$ at redshifts $z > 9$ is examined using constrained N-body simulations. The average specific mass accretion rates, $\dot{M}_{\rm h}/M_{\rm h}$, exhibit minimal mass dependence and generally agree with existing literature. Individual halo accretion histories, however, vary substantially. About one-third of simulations reveal an increase in $\dot{M}_{\rm h}$ around $z \approx 13$. Comparing simulated halos with observed galaxies having spectroscopic redshifts, we find that for galaxies at $z \gtrsim 9$, the ratio between observed star formation rate and $\dot{M}_{\rm h}$ is approximately 2%. This ratio remains consistent for the stellar-to-halo mass ratio (SHMR) but only for $z \gtrsim 10$. At $z \simeq 9$, the SHMR is notably lower by a factor of a few. At $z \gtrsim 10$, there is an agreement between specific star formation rates (sSFRs) and $\dot{M}_{\rm h}/M_{\rm h}$. However, at $z \simeq 9$, observed sSFRs exceed simulated values by a factor of 2. It is argued that the mildly elevated SHMR in high-z halos with $M_{\rm h} \approx 10^{11} M_\odot$ can be achieved by assuming the applicability of the local Kennicutt–Schmidt law and a reduced effectiveness of stellar feedback due to deeper gravitational potential of high-z halos of a fixed mass.

Unified Astronomy Thesaurus concepts: High-redshift galaxies (734); Galaxies (573); Star formation (1569)

1. Introduction

The standard ΛCDM cosmological model, incorporating a cosmological constant, Λ, and cold dark matter (DM), has been remarkably successful in interpreting and predicting fundamental properties of the large-scale structure of the Universe. Despite potential tensions (e.g., M. Asgari et al. 2021; A. G. Riess et al. 2023), this success extends to temperature anisotropies of the cosmic microwave background, clustering of the distribution of galaxies, and deviations of galaxy motions from a purely Hubble flow (e.g., S. Cole et al. 2005; D. J. Eisenstein et al. 2007; M. Davis et al. 2011; J. Carrick et al. 2015; Planck Collaboration et al. 2020; R. Lilow et al. 2021). On galactic scales, predicting the properties of the galaxy population and its evolution with redshift has been less straightforward. This complexity arises from the intricate nature of baryonic physics involved in star formation processes, including gas dynamics, heating and cooling mechanisms, and notably, the energetic feedback from supernovae (SNe) and active galactic nuclei (AGNs; e.g., R. B. Larson 1974; A. Dekel & J. Silk 1986; S. D. M. White & C. S. Frenk 1991; J. Silk & M. J. Rees 1998; P. Okalidis et al. 2021; M. R. Krumholz et al. 2018; A. Nusser & J. Silk 2022).

Prior to the era of the James Webb Space Telescope (JWST; J. P. Gardner et al. 2023), significant efforts have been invested in developing models of galaxy formation to adequately describe observations at low and moderately high redshifts ($z \lesssim 10$; e.g., S. L. Finkelstein et al. 2022).

Observations obtained with the JWST have significantly deepened our view of the Universe, revealing galaxies as far back as a couple of hundred million years near the Big Bang. However, the JWST has also detected an unexpected excess of luminous galaxies at higher redshifts. While the initial findings from the JWST appeared to pose serious challenges for the standard ΛCDM model of structure formation, the severity of these discrepancies was significantly alleviated with more precise calibration and the availability of spectroscopic redshifts (e.g., L. Y. A. Yung et al. 2024, for an overview).

It should be emphasized that the star formation rates (SFRs) in high-redshift JWST galaxies are not particularly unusual in themselves (e.g., B. E. Robertson et al. 2023; Y. Harikane et al. 2024). These galaxies exhibit SFRs that can be adequately sustained by cosmological gas accretion onto halos (C. A. Mason et al. 2023). Matching the abundance of halos to the observed distribution of UV magnitudes (used as proxies for the SFRs) of galaxies at $z \gtrsim 10$ implies that these galaxies should be hosted in halos of mass $M_{\rm h} \approx 5 \times 10^{10}$–$10^{11}\,M_\odot$ (M. Boylan-Kolchin 2023; C. A. Mason et al. 2023; Y. Chen et al. 2023). For such halos, the star formation efficiency $f_{\rm SF}$ (i.e., the fraction of accreting gas turning into stars) needed to account for the SFRs, is $\gtrsim$0.13 (see Section 3.2.1 below). At low redshifts ($z \lesssim 4$), the stellar-to-halo mass ratio (SHMR) inferred from abundance matching is in the range of 0.001–0.01 for $M_{\rm h} \approx 10^{11}\,M_\odot$ halos (e.g., B. P. Moster et al. 2013; A. Rodríguez-Puebla et al. 2017; G. Girelli et al. 2020; H. Fu et al. 2022). Assuming a global gas fraction of $f_{\rm b} = 0.157$ in galaxies (Planck Collaboration et al. 2020), this implies an average star formation efficiency, $f_{\rm SF} \approx 0.06$–0.006, which is at least a factor of 2 lower than the inferred value at $z \gtrsim 10$.

An important aspect of star formation inside DM halos is their mass accretion history (e.g., S. D. M. White & C. S. Frenk 1991). Halo accretion is directly linked to the availability of gas for star formation. Newly accreted gas replenishes the reservoir, which is subsequently converted into stars and may escape the galaxy through processes like SNe and AGN feedback. In this paper, we assume that $z \gtrsim 10$ galaxies indeed inhabit massive halos and aim to numerically investigate the assembly history of these halos. Numerical studies of individual objects typically rely on the methodology of zoom-in simulations (e.g., N. Katz et al. 1993; R. J. J. Grand et al. 2021; A. Pallottini & A. Ferrara 2023; G. Sun et al. 2023b). In this type of simulation, high resolution is employed only in a small region, allowing a detailed study of its smallscale dynamics while simultaneously capturing the interaction within the larger cosmic environment. In this paper, we invoke an alternative approach of constrained simulations (e.g., E. Romano-Diaz et al. 2005) to model the high-redshift $z > 9$ accretion history of halos above $M_{\rm h} \approx 10^{11}\, M_\odot$. We utilize the Y. Hoffman & E. Ribak (1991) method of constrained random realizations to generate initial conditions that are guaranteed to contain a halo in a specified mass range when evolved forward to a specified redshift, z.

The technique of constrained simulations is very useful in large-scale structure studies, especially for assessing uncertainties in parameter estimations realistically and in mitigating cosmic variance (W. A. Hellwing et al. 2017). This approach has been used to derive simulation initial conditions from the observed peculiar velocities (Y. Hoffman et al. 2015) and from the 2MRS redshift survey (R. Lilow et al. 2021). Initial conditions based on the galaxy distribution in the Sloan Digital Sky Survey have also been generated to run a constrained simulation to study the Local Universe (H. Wang et al. 2016). The same simulation has also been utilized to study the $z \simeq 0$ descendants of galaxies at $z \approx 8$–9 galaxies (Y. Chen et al. 2023).

The structure of the paper is outlined as follows. In Section 2, we assess the abundance of halos and compare it with the luminosity function (LF) of galaxies at high redshifts. We underscore the advantage of constrained simulations based on the expected abundance of the host halos. The simulations are detailed in Section 3, which includes the method for generating suitable initial conditions. Additionally, this section contrasts the accretion history of halos in the simulations with observational data. In Section 4, a straightforward recipe for star formation is introduced. The recipes produce a higher ratio of stellar-to-halo mass at high redshifts compared to low redshift. A summary and discussion are provided in Section 5.

We adopt the standard flat ΛCDM cosmological model (Planck Collaboration et al. 2020) with a total mass density parameter $\Omega_m = 0.311$, baryonic density $\Omega_b = 0.049$, Hubble constant $H_0 = 67.7\ {\rm km\ s^{-1}\ Mpc^{-1}}$, and normalization $\sigma_8 = 0.81$.

2. Halo Abundance at High Redshift

We employ a halo definition in terms of a spherical overdensity, where the halo virial radius $r_{\rm h}(t)$, at any given time t is determined such that the mean density within this radius equals 200 times the critical density of the universe, $\rho_c(t) = 3H(t)^2/8\pi G$. Therefore,

$$\begin{aligned} r_{\rm h}(t) &= 0.1H(t)^{-1}V_c, \\ M_{\rm h}(t) &= 0.1G^{-1}H(t)^{-1}V_c^3, \end{aligned} \tag{1}$$

where the circular velocity $V_{\rm c} = \sqrt{GM_{\rm h}/r_{\rm h}}$. At high redshifts where $H \sim 1/t$, these relations yield

$$\begin{aligned} r_{\rm h}(t) &= 13.1\ {\rm kpc}\left(\frac{11}{1+z}\right)^{3/2}\frac{V_c}{181\ {\rm km\ \ s^{-1}}}, \\ M_{\rm h}(t) &= 10^{11}\,{\rm M_\odot}\left(\frac{11}{1+z}\right)^{3/2}\left(\frac{V_c}{181\ {\rm km\ \ s^{-1}}}\right)^3. \end{aligned} \tag{2}$$

Figure 1 displays the abundance of DM halos per logarithmic mass bin per Mpc^3 at different redshifts. The plots are generated using the widely used halo mass function (HMF) outlined by J. Tinker et al. (2008; hereafter Tinker08) for the ΛCDM cosmological model, as incorporated within the COLOSSUS cosmology Python package (B. Diemer 2018). The curves corresponding to halos within the mass range $M_{\rm h} \gtrsim 10^{11}\, M_\odot$ at redshifts $z \gtrsim 9$ exhibit comparable abundance to large groups and clusters at $z = 0$. At the upper end of the mass range, the dependence on mass steepens significantly at such high redshifts. For instance, at $z = 9$, the abundance of halos with $M_{\rm h} = 10^{12}\, M_\odot$ is 4 orders of magnitude lower than halos with $M_{\rm h} = 10^{11}\, M_\odot$. A reasonable approximation to the HMF is given by

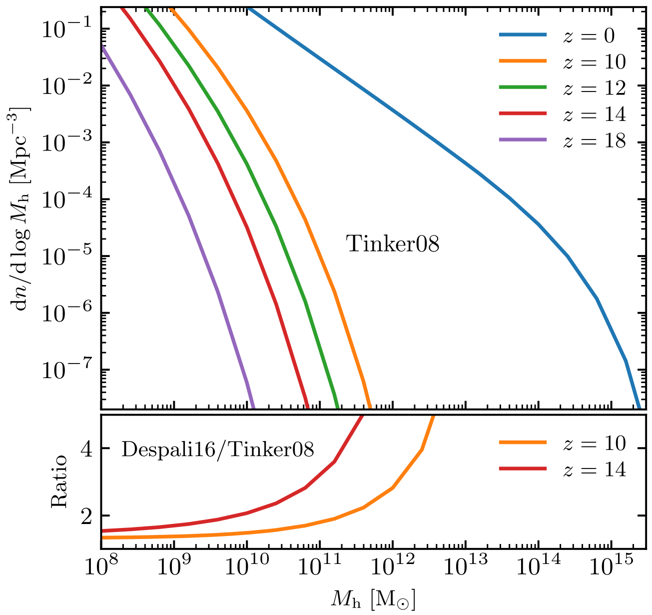

Figure 1. Top: halo abundance vs. mass at different redshifts as denoted in the figure. The solid lines are derived from the Tinker08 expression for the mass function in the Planck ΛCDM cosmology (see the main text). At the high mass end, the curves are $\sim M_{\rm h}^{-4}$ and thus the cumulative number density $n\,(>M_{\rm h}) \approx (1/4)dn/d\log M_{\rm h}$. Bottom: ratio of Despali16 to Tinker08 HMFs.

$$\frac{dn(z,\, M_{\rm h})}{d\,\log M_{\rm h}} = \frac{10^{-5}\ {\rm Mpc^{-3}}}{\left[\left(\frac{M_{\rm h}}{M_{-5}(z)}\right)^2 + 0.25\left(\frac{M_{\rm h}}{M_{-5}(z)}\right)^{0.8}(z)\right]^2}. \tag{3}$$

The approximation is valid in the redshift range $10 < z < 20$ with $M_{-5}(z)$ is defined as

$$\log\,(M_{-5}/10^{11}\, M_\odot) = 0.185(z - 10)^{1.03}, \tag{4}$$

and is equal to the halo mass where $dn/d\log M = 10^{-5}\ {\rm Mpc^{-3}}$. For $M \gtrsim M_{-5}(z)$, we have the steep dependence $dn/d\log M \sim M^{-4}$.

Various fitting formulae for the mass function are available in the literature (e.g., W. H. Press & P. Schechter 1974; R. K. Sheth & G. Tormen 1999; A. R. Jenkins et al. 2001; R. E. Angulo et al. 2012; R. Seppi et al. 2021). Therefore, it is important to investigate whether discrepancies among these mass functions might be particularly notable when applied to high redshifts. The bottom panel of Figure 1 compares the Tinker08 with another widely used HMF given in G. Despali et al. (2016; hereafter Despali16). The ratio between these HMFs increases with mass and redshift but remains within a factor of a few. Further, due to the steep dependence of the number density on halo mass, we shall see in Figure 2 that differences in the HMF lead to minor changes in the estimation of halo masses by matching UV LF.

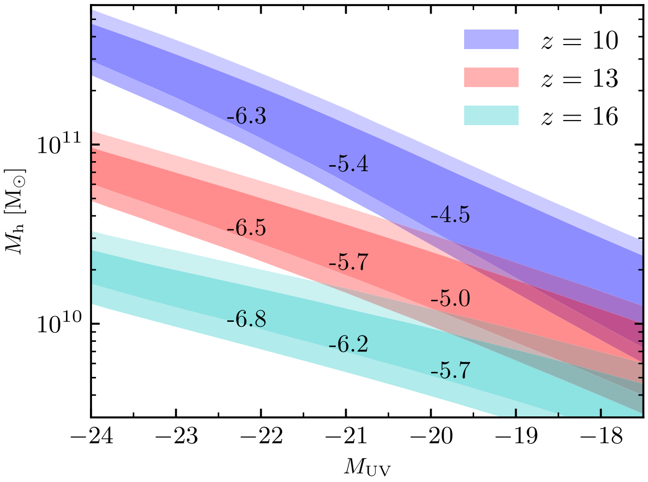

Figure 2. Halo mass vs. UV magnitude obtained by abundance matching of the Tinker08 (dark shaded areas) and Despali16 (light shades) HMF to the double power-law fit of H24 to UV LF, Φ_{UV}. Each shaded area corresponds to a single redshift and is bounded by M_h curves obtained using $5\Phi_{UV}$ (yielding the lower boundary of the shaded area) and by $0.2\Phi_{UV}$ (leading to the upper boundary). The numbers in each shaded area represent the log of the cumulative halo abundance (in Mpc^{-3}) expected at the corresponding M_{UV}.

2.1. Abundance Matching

Y. Harikane et al. (2024; hereafter H24) constrain the UV LF of high-z galaxies using 25 galaxies with spectroscopic redshifts spanning $z \approx 8.61$–13.20. Their constraints align with various luminosity distributions derived from photometric redshifts (e.g., C. T. Donnan et al. 2023; P. G. Pérez-González et al. 2023; R. J. Bouwens et al. 2023; Y. Harikane et al. 2023). H24 show that the observed UV LF can be effectively modeled by a double power-law function, denoted as Φ_{UV}.

Using this double power-law fit, we conduct a straightforward abundance matching to associate galaxies with a UV magnitude, M_{UV}, to halos of mass M_h The results are summarized in Figure 2 for three redshift values and for the HMFs of Tinker08 (dark shaded area) and Despali16 (light shaded). The width of each shaded area corresponds to variation in the normalization of the double power-law fit, spanning a factor between 0.2 and 5. While this should provisionally reflect the uncertainty in the measured UV LF of H24, it is important to note that the uncertainty in the observed luminosity in a single bin of 1 UV magnitude width could be as large as 2 orders of magnitude. The results for the Tinker08 and Despali16 HMFs are remarkably consistent. This consistency is due to the steep dependence of the mass function on the mass of rare halos, approximately $\sim M_h^{3.5-4}$, which implies weak sensitivity of M_h to the observed number of galaxies in a given UV bin.

At $M_{UV} = -21$, the halo mass is in the range of $M_h = 6 \times 10^{10}$–$1.5 \times 10^{11} M_\odot$ at $z = 10$, with a cumulative halo abundance (indicated by log the number density in the shaded areas) similar to massive groups and clusters at $z = 0$. Although galaxies with a fixed M_{UV} correspond to lower M_h as we move from low to high redshifts, the decrease in M_h is insufficient to maintain the same abundance. In fact, halos corresponding to a fixed M_{UV} become rarer.

At $z \approx 10$, on average a single halo with $M_h = 2 \times 10^{11} M_\odot$ is expected in a box a 100 Mpc. While it is possible to employ zoom-in techniques for simulating massive halos at $z \gtrsim 10$, this necessitates significant computational resources. Instead, we adopt a computationally friendlier approach, utilizing constrained random realizations to generate initial conditions that are guaranteed to contain a massive halo when evolved forward to a specified redshift, z.

3. Simulations

In Section 3.1, we outline the method for generating constrained initial conditions. Using these initial conditions, simulations of DM particles were conducted in periodic boxes using the SWIFT cosmological code (M. Schaller et al. 2024). All simulations started at redshift $z_i = 80$ and concluded at $z = 9$. As we shall see below, the linear density contrast corresponding to the constraint is $\delta_c = 1.68$ at $z = 9$, and hence, the corresponding density at the initial redshift z_i is 0.02, well within the linear regime. Furthermore, to capture any mild deviations from linear evolution at z_i, the initial conditions are generated using the Zel'dovich approximation rather than linear theory.

We performed nine simulations constrained to have halo masses of approximately $M_h \approx 10^{11} M_\odot$ in boxes of $L = 17.1$ Mpc, along with one unconstrained simulation in a box of the same size. Additionally, two simulations were conducted with initial conditions constrained to include a halo mass of $M_h \approx 10^{12} M_\odot$ at $z = 9$, positioned at the center of cubic boxes of $L = 36.9$ Mpc.

Each simulation consisted of 512^3 equal-mass particles, resulting in particle masses of $10^7 M_\odot$ and $10^6 M_\odot$ in the large and small boxes, respectively. The maximum physical softening used in the simulations was 100 pc. Throughout each simulation run, the output of positions and velocities of all particles was retained at 18 different redshifts spanning from $z = 20$ to $z = 9$. Halos were identified from the simulation outputs utilizing the VELOCIRAPTOR halo finder (P. J. Elahi et al. 2019). This halo finder provides halo masses according to several definitions. Here, we use VELOCIRAPTOR masses that match the definition in Equation (1).

3.1. Constrained Initial Conditions

We formulate the condition (constraint) for the presence of a halo of a given mass as follows. Let $\delta(\boldsymbol{x}, z)$ be the linearly evolved density at redshift z and $\delta_R(\boldsymbol{x}, z)$ be its convolution with a top-hat window of comoving radius R. We associate a halo of mass M_h with a comoving Lagrangian radius $R_L = (3M_h/4\pi\rho_m)^{1/3}$, where ρ_m is the background density in comoving coordinates.

The formation of a halo of mass M_h at redshift z, located at position $\boldsymbol{x}_0$ is determined by the condition $\delta_{R=R_L}(\mathbf{x}_0, z) = \delta_c \simeq 1.68$ (e.g., W. H. Press & P. Schechter 1974; P. J. E. Peebles 1980). Here, δ_c is the critical threshold indicative of the virialization of DM halos. At $z = 10$, halos with masses $M_h = 10^{11} M_\odot$ and $M_h = 10^{12} M_\odot$ correspond to Lagrangian comoving radii of $R_L = 0.84$ Mpc and 1.82 Mpc, respectively. In terms of the ratio δ_c/σ_{R_L}, these are equal to 4.8 and 6.5, providing a measure of halo formation likelihood under the specified conditions. This formulation is only approximate as the superposition of generic fluctuations on all scales and nonlinear evolution will lead to deviations from the desired halo mass and position. Nonetheless, the prescription is reasonable for massive (rare) halos (B. E. Robertson et al. 2009; A. D. Ludlow et al. 2014), as is the case in the current study.

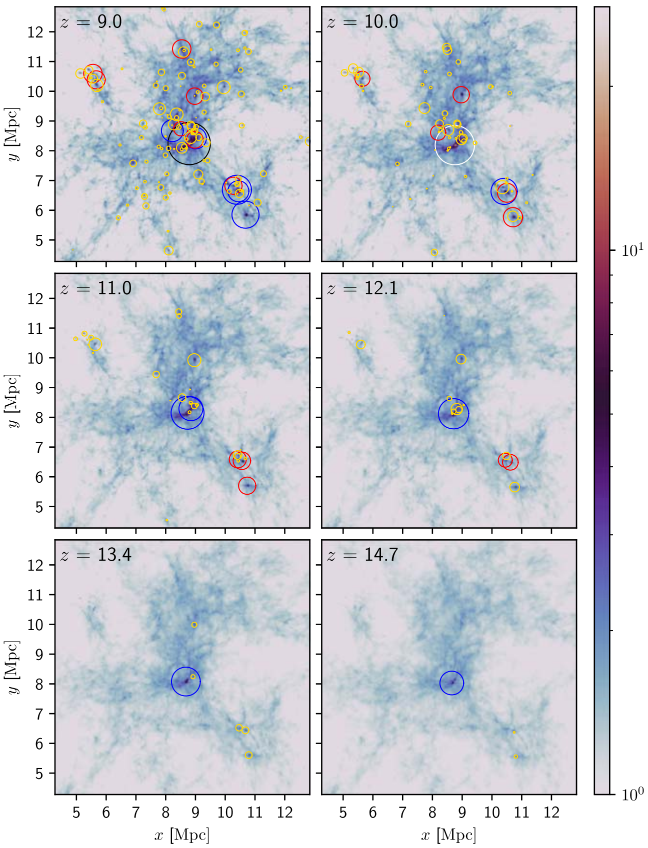

Figure 3. Projected 2D density field from one of the constrained simulations with $L = 17.1$ Mpc at six distinct redshifts. Circles denote halos classified by mass ranges: black ($M_{\rm h}/M_\odot > 10^{11}$), white ($5 \times 10^{10}$–$10^{11}$), blue ($10^{10}$–$5 \times 10^{10}$), red ($5 \times 10^9$–$10^{10}$), and yellow ($10^9$–$5 \times 10^9$), with size logarithmically scaled by mass. The color bar indicates density relative to the mean density within the simulation box.

We adopt the methodology of Y. Hoffman & E. Ribak (1991) to generate Gaussian random fields that satisfy the aforementioned condition. This method expresses the constrained random field, denoted by δ_1, in terms of an unconstrained random Gaussian field, $\delta^{\rm unc}$, as follows:

$$\delta_1(\boldsymbol{x}, z) = \delta^{\rm unc}(\boldsymbol{x}, z) - \langle \delta(\boldsymbol{x}, z) | \delta^{\rm unc}_{R_L} \rangle + \langle \delta(\boldsymbol{x}, z) | \delta_c \rangle \ , \quad (5)$$

where $\delta^{\rm unc}_{R_L}$ is the value of the filtered unconstrained field at $\boldsymbol{x}_0$. The ensemble average of all δ fields satisfying the constraint $\delta_{R_L}(\boldsymbol{x}_0, z) = C$ is given by

$$\langle \delta(\boldsymbol{x}) | C \rangle = \zeta(|\boldsymbol{x} - \boldsymbol{x}_0|) \frac{C}{\sigma^2_{R_L}}, \quad (6)$$

where $\sigma^2_{R_L}$ is the variance of the smoothed density, δ_{R_L}.

3.2. Results

Figure 3 illustrates the projected (2D) density (in units of the mean 2D density value) for one of the $M_{\rm h} = 10^{11} M_\odot$ constrained simulations. The overlaid circles represent identified halos in different mass ranges, as described in the figure caption. Only halos above $10^9 M_\odot$ are marked.

The displayed region of the box is focused around the center. As expected, the most massive halo (MMH) forms near the center. Additional massive halos are associated with the growth of the MMH, however, their masses are significantly lower than the MMH. Halos in the mass range of $5 \times 10^9 < M_{\rm h}/M_\odot < 10^{10}$ (red circles) are present at $z \simeq 12$. These halos are not considered rare, as their expected abundance is 10^{-2}–10^{-3}dex^{-1} Mpc^{-3} (see Figure 1). Therefore, we expect to identify a few such halos even in our simulation box of $L = 17.1$ Mpc.

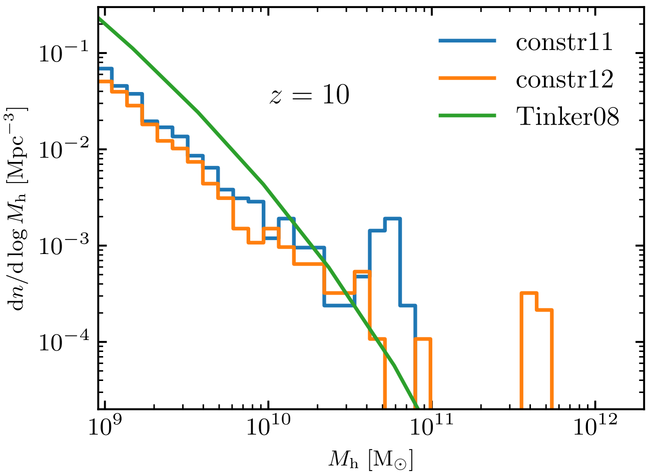

Figure 4. Halo abundance computed from the output of the simulations at $z = 9$. The blue and orange histograms represent the constrained simulations with halo masses of $10^{11} M_\odot$ and $10^{12} M_\odot$, respectively. The green curve depicts the Tinker08 mass function.

Inspection of the panels at $z = 11$ and $z = 10$ reveals a major merger event with the two halos marked by two blue circles ($10^{10} < M_{\rm h}/M_\odot < 5 \times 10^{10}$) at $z = 11$ merging to form the larger halo indicated by the white circle ($5 \times 10^{10} < M_{\rm h}/M_\odot < 10^{11}$) at $z = 10$. There is a clear tendency of increasing halo mass as we move nearer to the MMH, particularly at the lowest redshifts.

Figure 4 shows the abundance of halos from the simulations as a function of $M_{\rm h}$. At the high mass end, the simulated abundance significantly exceeds the predictions from the Tinker08 fitting formula (green curve). In both $M_{\rm h} = 10^{11} M_\odot$ and $M_{\rm h} = 10^{12} M_\odot$ constrained simulations, the MMH is accompanied by other relatively rare massive halos with abundance well above the green curve. The initial condition constraint ensures a massive halo in a small region, making the simulation box atypical for its volume. Consequently, the number density of massive halos in the simulation significantly exceeds the expected mean, explaining the enhanced abundance of high $M_{\rm h}$ halos compared to Tinker08. One pathway for the formation of these massive halos is through the accretion of smaller halos, leading to a modest depletion in the low $M_{\rm h}$ range. This explains why the simulated halo abundance at low $M_{\rm h}$ falls slightly below the green curve, typically by a factor of 3–4.

3.2.1. Halo Accretion History

Figure 5 displays the evolution of MMH properties in simulations (continuous curves) and compares them with observational data (individual symbols). The figure is divided into three panels, each focusing on a different aspect of halo growth. The data symbols are as follows.

1. *Magenta symbols with error bars* are based on stellar masses and SFRs inferred via spectral energy distribution (SED) fitting. The *filled squares* are taken from Table 3 in H24. The *open squares* refer to the galaxy GS-z12 for

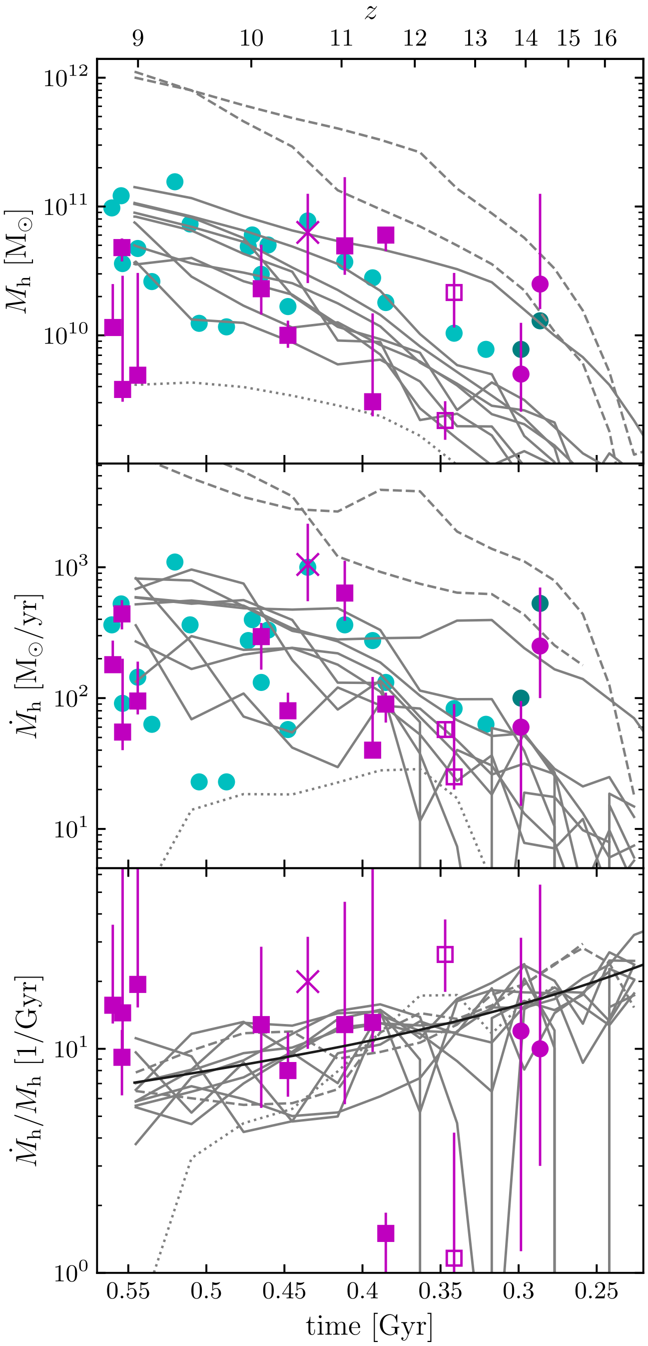

Figure 5. Accretion histories of main halos in unconstrained (dotted) and constrained simulations with $M_h = 10^{11}\,M_\odot$ (solid) and $10^{12}\,M_\odot$ (dashed). Observational data shown as magenta and cyan symbols. Top: halo mass vs. time. Magenta: derived from SED-fitted M_* in the literature, assuming $M_{\rm h} = 50M_*$ (see Equation (7)). Cyan: from abundance matching of observed $M_{\rm UV}$. Middle: Accretion rate $\dot{M}_h$. Magenta: $\dot{M}_{\rm h} = 50\dot{M}_*$ from observed SED-fitted $\dot{M}_*$. Cyan: from UV-estimated $\dot{M}_*$. Bottom: curves of specific accretion rate $\dot{M}_{\rm h}/M_{\rm h}$, with the fit $\sim t^{-4/3}$ plotted in black, and observed sSFR $\dot{M}_*/M_*$ shown as magenta points. See text for details.

which different values of redshift, SFR, and M_* are reported in F. D'Eugenio et al. (2024) and H24. Both sets of data are shown, with F. D'Eugenio et al. (2024) being the point with the lower redshift ($z = 12.43$). The *cross* is the galaxy GN-z11 (S. Tacchella et al. 2023). The two highest redshift points represented by *filled circles* correspond to the two galaxies reported in S. Carniani et al. (2024).

The observed stellar mass, M_*, and SFRs, $\dot{M}_*$, are used to estimate halo masses and mass accretion rates assuming assuming

$$M_{\rm h} = f_{\rm b}^{-1} f_{\rm SF}^{-1} M_* = 50\left(\frac{0.13}{f_{\rm SF}}\right) M_*, \tag{7}$$

and similarly for the relation between $\dot{M}_{\rm h}$ and $\dot{M}_*$. As before, f_b is the global baryonic mass fraction, and the star formation efficient $f_{\rm SF}$ is a constant assigned a default value $f_{\rm SF} = 0.13$, implying $M_{\rm h} = 50M_*$

2. *Cyan circles* are based solely on the observed $M_{\rm UV}$ provided in Table 1 of H24. The *dark cyan circles* correspond to the two highest redshift galaxies, with $M_{\rm UV}$ taken from S. Carniani et al. (2024). For these points, halo masses are inferred from $M_{\rm UV}$ via abundance matching from the observed UV magnitudes. From Figure 2, the relative uncertainty in these points is a factor of ≈2–3, but we do not attach the corresponding error bars for the sake of clarity. The SFRs are deduced directly using $\dot{M}_*(M_\odot\,{\rm yr}^{-1}) = 1.15 \times 10^{-28} L_{\rm UV}({\rm erg\ s^{-1}\,Hz^{-1}})$ assuming a Salpeter initial mass function (IMF). The halo accretion rate is them estimated from Equation (7).

Top panel: halo mass versus time. The gray curves correspond to $M_{\rm h}(t)$ of the simulated MMHs. The curves reveal that half of the simulated MMHs, including the unconstrained halo (dotted), have acquired 80% of their final masses in the last 150 Myr. Only the dashed curves, corresponding to constrained simulations with $M_{\rm h} \approx 10^{12}\,M_\odot$ and one of the nine solid curves, have acquired a mass $\gtrsim 10^{10}\,M_\odot$ by $z = 15$.

The *cyan circles* fall within the range of solid curves corresponding to simulations constrained to contain a $M_{\rm h} \approx 10^{11}$ halo. The result is not entirely trivial since $M_{\rm h}$ of the MMHs been tuned to match the abundance at redshifts $z \approx 9$ and not at higher redshifts. Indeed, at higher redshifts, the spread in halo masses between different simulations is becomes large, ranging from $M_{\rm h} \approx 10^{10}\,M_\odot$ to $10^{11}\,M_\odot$ even at at $z = 10$, as indicated by the solid curves. This mass range is associated with more than a 2 order-of-magnitude difference in the abundance of halos, as shown in Figure 1.

The highest redshift data point represented by a *magenta circle* is well above all solid curves except one (yellow curve). Nonetheless, since we have only nine curves corresponding to the $M_{\rm h} = 10^{11}\,M_\odot$ simulations, we conclude that this data point is consistent with simulated accretion history.

At $z \gtrsim 10$, the estimates from Equation (7) (magenta) agree with both the $M_{\rm h} = 10^{11}\,M_\odot$ simulations and abundance matching results (cyan circles). However, at $z \simeq 9$, these estimates fall below both simulations and abundance matching. This is in agreement with various models in the literature (e.g., P. S. Behroozi & J. Silk 2015; V. Mauerhofer & P. Dayal 2023; L. Y. A. Yung et al. 2024; Y. Harikane et al. 2024) predicting an LF consistent with the observations at $z \lesssim 9$, but underestimating the observed abundances at $z \gtrsim 11$.

Middle panel: mass accretion rate. As in the previous panel, the curves correspond to the simulations. The $\dot{M}_{\rm h}$ curves reveal significant variations between individual halos. Some halos exhibit highly fluctuating $M_{\rm h}$, while others (e.g., those represented by dashed and a few solid curves) show smoother evolution. However, even these smoother curves display fluctuations on timescales $\lesssim$100 Myr.

The magenta and cyan points agree with each other, but are not identical, as the SED fitting involves more detailed SFR modeling than UV magnitudes alone. Accretion rate curves from the $M_{\rm h} = 10^{11}\,M_\odot$ simulations are consistent with observations via $M_{\rm UV}$ (cyan) and SED SFRs (magenta).

We emphasize that while both cyan and magenta points in top and middle panels rely on $M_{\rm UV}$, their methodologies differ: abundance matching for the top panel versus an empirical SFR–$M_{\rm UV}$ relationship for the middle panel.

Bottom panel: specific accretion rate. The specific halo accretion rates, $\dot{M}_{\rm h}/M_{\rm h}$, from simulations cluster around a simple fit denoted by a black line, represented by the equation $d\ln M_{\rm h}/dt = 3.15 t_{\rm Gyr}^{-4/3}\ {\rm Gyr}^{-1}$. This fit approximates the mean accretion rate for halos of mass $M_{\rm h} = 10^{11}\,M_\odot$ as proposed by O. Fakhouri et al. (2010).

The magenta points represent the specific star formation rate (sSFR), $\dot{M}_*/M_*$, from observations. Cyan circles are absent from this panel since only $\dot{M}_*$ can be directly derived from $M_{\rm UV}$.

At $z > 10$, there is a reasonable agreement between the observed sSFRs and the halo accretion rates from the simulations. This consistency corroborates the findings of R. J. Bouwens et al. (2023), who noted that the sSFRs tend to follow the scaling $(1+z)^{2.5}$ proposed by O. Fakhouri et al. (2010) for the specific halo accretion rate at high redshift. However, the normalization of the specific halo accretion rate in R. J. Bouwens et al. (2023) is higher by a factor of a few compared to the fit by O. Fakhouri et al. (2010).

At $z < 9$, the discrepancy between data and observations seen on the top panel is also evident here. While reducing $f_{\rm SF}$ by a factor of $\approx$5–10 (from $f_{\rm SF} = 0.13$ to 0.01–0.025) would reconcile the $z \simeq 9$ with the $M_{\rm h}$ results in the top panel, it would not effect the halo specific accretion rate (assuming a constant $f_{\rm SF}$). The is because, according to Equation (7), the specific accretion rate is equal to the sSFR, i.e., $\dot{M}_{\rm h}/M_{\rm h} = \dot{M}_*/M_*$, independently of $f_{\rm SF}$.

Note that $M_* \propto M_{\rm h}^{\alpha}$ ($\alpha = {\rm const}$), then $\dot{M}_{\rm h}/M_{\rm h} = \alpha^{-1}\dot{M}_*/M_*$ (P. S. Behroozi & J. Silk 2015). Therefore, also for $\alpha \neq 1$ curves of the sSFR and the specific halo accretion rate should trace each other, with a constant ratio between them. Thus, a mass-dependent $f_{\rm SF}$ would not resolve the discrepancy.

4. Boosting the Star Formation Efficiency at High-*z*

A boost in $f_{\rm SF}$ to $\approx$0.13 at high-*z* yields reasonable agreement between simulated halos and observations, representing a mild increase relative to low-*z*. We present a simple recipe explaining this enhancement, suggesting that star formation processes may not significantly differ across redshifts. We present a model explaining this enhancement, arguing that star formation processes may not significantly differ across redshifts. For a halo of mass $M_{\rm h}(t_z)$ at redshift z, we model M_* and $\dot{M}_*$ assuming star formation occurs in a rotationally supported disk governed by the Schmidt–Kennicutt (SK) law (M. Schmidt 1959; R. C. Kennicutt 1998):

$$\dot{\Sigma}_* = A\Sigma_g^n, \tag{8}$$

where $\dot{\Sigma}_*$ is the SFR per unit disk area, $n = 1.54$, and $A = 10^{-3.95}$ (R. C. Kennicutt & M. A. C. De Los Reyes 2021). Σ_* and Σ_g are in $M_\odot$ pc^{-2}. Disk gas partially converts to stars following the SK law, with stellar feedback expelling a fraction. The disk gas reservoir is simultaneously replenished and expanded through halo accretion.

The gas surface density evolution is described by

$$\dot{\Sigma}_g = \dot{\Sigma}_{\rm acc} - \dot{\Sigma}_* - \dot{\Sigma}_{\rm ej}, \tag{9}$$

where $\dot{\Sigma}_{\rm acc}$ is accretion, $\dot{\Sigma}_*$ is star formation, and $\dot{\Sigma}_{\rm ej}$ is feedback-driven ejection. For halos with $M_{\rm h} \lesssim 10^{12} M_\odot$, AGN feedback is subdominant (D. J. Croton et al. 2006; R. G. Bower et al. 2006; E. Puchwein & V. Springel 2013).

Gas ejection is modeled via (S. D. M. White & C. S. Frenk 1991; G. Kauffmann et al. 1993; P. D. Mitchell et al. 2018; L. Y. A. Yung et al. 2019),

$$\dot{\Sigma}_{\rm ej} = \left(\frac{V_c}{V_{\rm SN}}\right)^{-\gamma}\dot{\Sigma}_*, \tag{10}$$

with $V_{\rm SN} = 240$ km s^{-1} and $\gamma = 2.8$ (L. Y. A. Yung et al. 2019). This implies more effective stellar feedback in halos with shallow gravitational potential (R. B. Larson 1974; A. Dekel & J. Silk 1986).

The accreted gas mass in time δt is

$$\delta M_{\rm acc} = f_{\rm b}\dot{M}_{\rm h}\delta t. \tag{11}$$

Due to short crossing times and efficient cooling (A. Dekel et al. 2023; L. Y. A. Yung et al. 2024), we assume rapid settling into an exponential disk:

$$\delta\Sigma_{\rm acc}(t, R) = \delta\Sigma_0 e^{-R/R_d(t)}, \tag{12}$$

where $R_{\rm d} = 0.7\lambda_{\rm B} r_{\rm h}$ (H. J. Mo et al. 1998; H. Yang et al. 2023), and $\lambda_{\rm B}$ is the halo spin parameter (J. S. Bullock et al. 2001). Therefore,

$$\dot{\Sigma}_{\rm acc}(t, R) = \frac{f_{\rm b}\dot{M}_{\rm h}}{2\pi R_{\rm d}^2(t)} e^{-R/R_{\rm d}(t)}. \tag{13}$$

Motivated by our simulations, we assume $\dot{M}_{\rm h}/M_{\rm h} \propto t^{-4/3}$, yielding

$$M_{\rm h}(t) = M_{\rm h}(t_z) e^{A(t_z^{-\beta} - t^{-\beta})}, \tag{14}$$

where $A = -8.1$, $\beta = 1/3$, and t is in Gyr.

We numerically integrate Equations (8) and (13) from $t = t_i \ll t_z$ to $t = t_z$. Initial conditions are set as $\Sigma_*(t_i, R) = 10^{-3}\Sigma_g(t_i, R)$, with $\Sigma_g(t_i, R)$ following an exponential profile. $R_{\rm d}(t_i)$ is determined by $R_{\rm d} = 0.7\lambda_{\rm B} r_{\rm h}$ with $r_{\rm h} = r_{\rm h}(t_i)$. The initial disk gas mass equals $f_{\rm b} M_{\rm h}(t_i)$ minus the initial stellar mass. We use $\lambda_{\rm B} = 0.035$ in all calculations.

In the top panel of Figure 6, the SHMR is plotted against halo mass for four redshift values, z. The model agrees reasonably well with the observed local SHMR as estimated through abundance matching techniques (e.g., B. P. Moster et al. 2013; A. Rodríguez-Puebla et al. 2017; B. P. Moster et al. 2020; G. Girelli et al. 2020; M. Shuntov et al. 2022).

The model SHMR acquires larger values at higher redshifts for a given mass. This is due to the relation $V_c \sim M_{\rm h}/t$, indicating that a higher circular velocity V_c occurs at earlier times for a fixed $M_{\rm h}$, leading to less efficient SNe feedback and, consequently, a larger gas reservoir for star formation. The SHMR for $M_{\rm h} \approx 10^{11}\,M_\odot$ increases by approximately a factor of 5 at high-*z* compared to $z = 0$, while for $10^{10}\,M_\odot$, the increase is about a factor of 25. In contrast, predictions from the

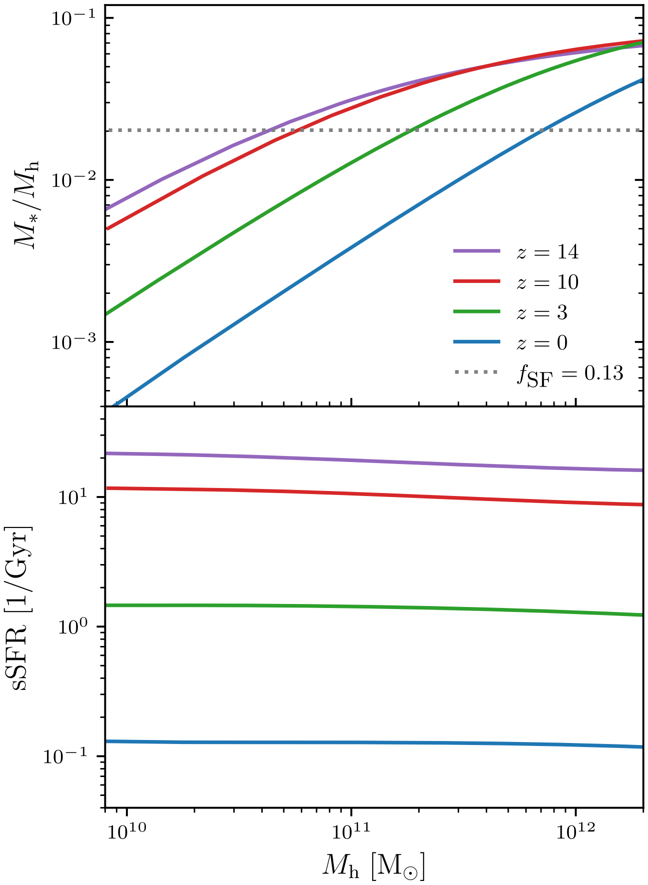

Figure 6. The SHMR (top panel) and the sSFR (bottom panel) from the simplified recipe in Section 4 at four different redshifts, as indicated in the figure. The dotted gray horizontal line indicates the value corresponding to $M_*/M_\mathrm{h} = f_\mathrm{SF} f_\mathrm{b}$ obtained with $f_\mathrm{SF} = 0.13$.

UNIVERSEMACHINE (P. Behroozi et al. 2020) suggest that the SHMR increases by about a factor of 10 from $z = 0$ to $z = 12$ for halos with $10^{10}\,M_\odot$ (their Figure 12).

The SHMRs change very little between $z = 10$ and 14 with a weak dependence on M_h. For the relevant mass range $M_\mathrm{h} \approx 5 \times 10^{10}$–$10^{11}\,M_\odot$ the SHMR is ≈2% corresponding to $f_\mathrm{SF} \approx 0.13$, the value used in figure Figure 5.

For $M_\mathrm{h} \approx 10^{11}\,M_\odot$, at $z = 3$, the SHMR changes by a factor of ≈4–5 compared to $z = 0$. This may seem at odds with observational analyses in the literature, which generally suggest a constant SHMR over this redshift range. We defer a detailed discussion of this issue to Section 5.

The sSFRs plotted in the bottom panel are close to the observed values at the corresponding redshifts (R. J. Bouwens et al. 2023) and depends weakly on M_h.

These results suggest that the enhanced star formation efficiency in high-z galaxies can be explained by the fundamental physics of structure formation and feedback processes, without invoking drastically different star formation mechanisms compared to the local universe.

5. Summary and Discussion

We have presented a study of the accretion history of massive halos at redshifts $z \gtrsim$, relevant to luminous galaxies observed at such high redshifts. Our approach is based on constrained simulations, which is highly beneficial for studying rare cosmological structures. Here, we have only conducted simulations with constant resolution across the entire simulation box. However, a combination of zoom-in techniques and constrained initial conditions is most appropriate for resolving rare structures as well as capturing the gravitational influence of the large-scale environment.

Growing evidence suggests highly variable star formation history at high redshifts (J. W. Cole et al. 2023; A. Dressler et al. 2024), potentially due to mergers, interactions, and environmental conditions. This variability could bias inferred UV luminosity distributions (K. Ren et al. 2019; C. A. Mason et al. 2023; G. Sun et al. 2023a, 2023b; X. Shen et al. 2023), as galaxies in low-mass halos may be preferentially detected during increased star formation phases. In the simulations, individual halo accretion curves exhibit both long-term fluctuations ($\gtrsim$100 Myr) and short-term variations. Examining Figure 5 (middle panel) reveals a tendency for greater variability in lower mass halos at $z = 9$ compared to more massive ones, potentially leading to enhanced stochasticity in associated SFRs. However, our output times do not capture variability at $\lesssim$10 Myr scales.

High-resolution simulations yield mixed results: SERRA simulations do not produce sufficient SFR variability (A. Pallottini & A. Ferrara 2023), while FIRE-2 simulations show bursty star formation that explains the observed UV LF (G. Sun et al. 2023b). However, stellar masses at $z \gtrsim 10$ in these simulations (X. Ma et al. 2018) are lower than observed estimates from spectroscopically confirmed galaxies (Y. Harikane et al. 2024). Nonetheless, stochasticity is clearly an important effect that should be considered.

In Figure 5 we have seen that dividing the observed SFRs by a factor of $f_b f_\mathrm{SF} = 2\%$ (i.e., $f_\mathrm{SF} = 0.13$), leads to $\dot{M}_\mathrm{h}$ that are consistent with the simulations constrained to include a halo of mass $M_\mathrm{h} \approx 10^{11}\,M_\odot$. The agreement spans the entire considered redshift range, $z > 9$. Interestingly, dividing the observed stellar masses by the same factor yields a good match with the halo masses in the simulations, but this is only true for $z \gtrsim 10$. For galaxies at $z \simeq 9$, the factor required is smaller by a factor of ≈5–10 ($f_\mathrm{SF} \approx 0.025$–$0.01$), closer to what is seen in low-redshift galaxies.

This peculiar behavior of the inferred M_h between $z \approx 9$ and $z \approx 10$ may stem from challenges in accurately estimating the stellar masses. Indeed, SFRs estimated from UV magnitudes are generally more reliable than stellar mass estimates, which require assumptions about the entire star formation history (e.g., L. Whitler et al. 2023) and SED fitting (V. Mauerhofer & P. Dayal 2023; A. Pallottini & A. Ferrara 2023; L. Whitler et al. 2023; C. Pacifici et al. 2023; B. Wang et al. 2023). A striking example is the galaxy GS-z12 ($z = 12.48$). Its estimated mass varies by an order of magnitude depending on the method used: $M_* = 4.3^{+1.8}_{-2} \times 10^8\,M_\odot$ using PROSPECTOR (B. D. Johnson et al. 2021; Y. Harikane et al. 2024) and $M^* = 4.36^{+1.8}_{-1.27} \times 10^7\,M_\odot$ using BEAGLE (J. Chevallard & S. Charlot 2016; F. D'Eugenio et al. 2024). Nonetheless, in estimating the SFRs, the impact of potential uncertainties due to potential dust attenuation needs to be assessed (e.g., R. C. Kennicutt et al. 2012). However, dust attenuation is expected to be small in these high-redshift galaxies (e.g., R. J. Bouwens et al. 2023), suggesting that the observed discrepancies could primarily be due to the complexities of stellar mass estimation.

Another possibility for this behavior is an abrupt change in the conditions for star formation at $z \approx 9$–10, similar to the suggestion of J. Silk et al. (2024) although their model refers to transition at $z \approx 6$.

Numerical simulations are computationally intensive for tracing the accretion history of a large ensemble of halos. Semi-analytic methods for generating constrained merger histories (E. O. Nadler et al. 2023) offer a CPU-efficient alternative. These could be valuable for exploring variations in past accretion rates of rare halos at high redshifts. Currently, these methods have been applied to trace the growth of rare halos from $z \approx 12$ to $z = 0$, rather than tracing rare halos at $z \approx 10$ backward in time.

Numerous models aim to understand the formation of luminous high-z galaxies. Y. Harikane et al. (2023) suggested that UV-inferred SFRs might be overestimated due to a top-heavy IMF at high redshift, which could arise naturally in low-metallicity environments. L. Y. A. Yung et al. (2024) noted this could account for a factor of 4 boost in UV luminosities, aligning their semi-analytic models with observations. A. Dekel et al. (2023) propose conditions for feedback-free star formation in $\approx 10^7\,M_\odot$ gas clouds at high redshifts, satisfied in $10^{11}\,M_\odot$ halos at $z \approx 10$. Conversely, J. Silk et al. (2024) invoke AGN positive feedback, suggesting short-lived AGN activity triggers vigorous star formation via momentum-conserving outflows. They predict a transition to energy-conserving flows at $z \approx 6$, leading to gas depletion and quenched star formation at lower redshifts. A. Ferrara et al. (2023) propose that decreased dust attenuation at high redshifts could explain the abundance of $z \gtrsim 10$ galaxies, compensating for reduced host halo abundance. Modifications to the primordial mass power spectrum have also been explored (H. Padmanabhan & A. Loeb 2023; P. Parashari & R. Laha 2023; N. Sabti et al. 2024; S. Hirano & N. Yoshida 2024).

In the approximate star formation recipe outlined in Section 4, we used the halo's circular velocity, V_c, as the parameter governing SNe feedback. Combined with the local Kennicutt–Schmidt law, the recipe aims to demonstrate that negative feedback at high-z is naturally expected to be less efficient than at lower z.

According to Figure 6 the recipe implies an evolving SHMR at moderate redshifts and a nonevolving one at $z \gtrsim 10$. Observationally, within the uncertainties, a nonevolving SHMR is generally consistent with galaxy luminosity distributions up to $z \lesssim 5$. However, for the redshift range $z \approx 0$–10, studies in the literature show divergent results. Some find weak to moderate redshift dependence (B. P. Moster et al. 2013, 2020; C. A. Mason et al. 2015; A. Rodríguez-Puebla et al. 2017; M. Stefanon et al. 2021), while others report significant evolution (P. S. Behroozi et al. 2013; G. Sun & S. R. Furlanetto 2016; P. Behroozi et al. 2019). Notably, substantial differences exist between various SHMR estimates at similar redshifts and halo masses.

The evolution of the SHMR, inferred through abundance matching techniques, is sensitive to various factors, including the shape of the galaxy's stellar mass function (X. Yang et al. 2012). As highlighted by H. Fu et al. (2022), uncertainties in observed stellar mass functions at redshifts $z \lesssim 4$ can lead to differing interpretations regarding the evolution of the SHMR from $z = 0$ to $z = 4$. Depending on specific assumptions about the stellar mass function, the SHMR could exhibit either a decrease or an increase over this redshift range. Depending on the assumptions, the SHMR for a halo with $M_{\rm h} \approx 10^{11}\,M_\odot$ could vary by 2 orders of magnitude due to different assumptions.

The recipe in Section 4 can be adapted to yield a nearly nonvarying SHMR at $z \lesssim 5$ through several modifications. For example, the adopted expression for $M_{\rm h}(t)$ is approximate and neglects variations between halos, which can be significant according to Figure 5. The expression motivated by our high-z simulation results. A recipe with slower accretion at moderate redshifts would yield a less varying SHMR at $z \lesssim 5$.

Furthermore, following L. Y. A. Yung et al. (2019), we have adopted a gas ejection expression determined by V_c. However, the maximum circular velocity (the peak of the rotation curve), $V_{\rm max}$, is likely more relevant since it better reflects the depth of the gravitational potential of the halo.

In the regime of stable clustering, $V_{\rm max}$ is expected to remain constant over long cosmic epochs. Thus, employing $V_{\rm max}$ instead of V_c in the model should result in a more constant SHMR over extended periods. We have run the recipe with $V_{\rm max}$ instead of V_c in Equation (10), where the dependence on $M_{\rm h}$ and z follows the formula obtained by A. Rodriguez-Puebla et al. (2016) by fitting the median growth of halos in MultiDark N-body simulations. This has yielded closer curves for the SHMR at $z = 0$ and $z = 3$, while leaving the curves at $z = 10$ and 14 virtually unchanged.

Acknowledgments

The author has benefited from fruitful conversations with Andrew Benson, Enzo Branchini, Stephane Charlot, Avishai Dekel, and Joe Silk. This research is supported by a grant from the Israeli Science Foundation number 893/22 and a grant from the Asher Space Research Institute. The research in this paper made use of the SWIFT open-source simulation code (http://www.swiftsim.com; M. Schaller et al. 2018) version 1.0.0.

Data Availability

New numerical simulation data have been generated and analyzed.

ORCID iDs

Adi Nusser https://orcid.org/0000-0002-8272-4779

References

Angulo, R. E., Springel, V., White, S. D. M., et al. 2012, MNRAS, 426, 2046
Asgari, M., Lin, C. A., Joachimi, B., et al. 2021, A&A, 645, A104
Behroozi, P., Conroy, C., Wechsler, R. H., et al. 2020, MNRAS, 499, 5702
Behroozi, P., Wechsler, R. H., Hearin, A. P., & Conroy, C. 2019, MNRAS, 488, 3143
Behroozi, P. S., & Silk, J. 2015, ApJ, 799, 32
Behroozi, P. S., Wechsler, R. H., & Wu, H.-Y. 2013, ApJ, 762, 31
Bouwens, R. J., Stefanon, M., Brammer, G., et al. 2023, MNRAS, 523, 1036
Bower, R. G., Benson, A. J., Malbon, R., et al. 2006, MNRAS, 370, 645
Boylan-Kolchin, M. 2023, NatAs, 7, 731
Bullock, J. S., Dekel, A., Kolatt, T. S., et al. 2001, ApJ, 555, 240
Carniani, S., Hainline, K., D'Eugenio, F., et al. 2024, Natur, 633, 318
Carrick, J., Turnbull, S. J., Lavaux, G., & Hudson, M. J. 2015, MNRAS, 450, 317
Chen, Y., Mo, H. J., & Wang, K. 2023, MNRAS, 526, 2542
Chevallard, J., & Charlot, S. 2016, MNRAS, 462, 1415
Cole, J. W., Papovich, C., Finkelstein, S. L., et al. 2023, arXiv:2312.10152
Cole, S., Percival, W. J., Peacock, J. A., et al. 2005, MNRAS, 362, 505
Croton, D. J., Springel, V., White, S. D. M., et al. 2006, MNRAS, 365, 11
Davis, M., Nusser, A., Masters, K. L., et al. 2011, MNRAS, 413, 2906

Dekel, A., Sarkar, K. C., Birnboim, Y., Mandelker, N., & Li, Z. 2023, MNRAS, 523, 3201
Dekel, A., & Silk, J. 1986, ApJ, 303, 39
Despali, G., Giocoli, C., Angulo, R. E., et al. 2016, MNRAS, 456, 2486
D'Eugenio, F., Maiolino, R., Carniani, S., et al. 2024, A&A, 689, A152
Diemer, B. 2018, ApJS, 239, 35
Donnan, C. T., Mcleod, D. J., Dunlop, J. S., et al. 2023, MNRAS, 518, 6011
Dressler, A., Rieke, M., Eisenstein, D., et al. 2024, ApJ, 964, 150
Eisenstein, D. J., Seo, H.-J., Sirko, E., & Spergel, D. N. 2007, ApJ, 664, 675
Elahi, P. J., Canas, R., Poulton, R. J. J., et al. 2019, PASA, 36, e021
Fakhouri, O., Ma, C.-P., & Boylan-Kolchin, M. 2010, MNRAS, 406, 2267
Ferrara, A., Pallottini, A., & Dayal, P. 2023, MNRAS, 522, 3986
Finkelstein, S. L., Bagley, M., Song, M., et al. 2022, ApJ, 928, 52
Fu, H., Shankar, F., Ayromlou, M., et al. 2022, MNRAS, 516, 3206
Gardner, J. P., Mather, J. C., Abbott, R., et al. 2023, PASP, 135, 068001
Girelli, G., Pozzetti, L., Bolzonella, M., et al. 2020, A&A, 634, A135
Grand, R. J. J., Marinacci, F., Pakmor, R., et al. 2021, MNRAS, 507, 4953
Harikane, Y., Nakajima, K., Ouchi, M., et al. 2024, ApJ, 960, 56
Harikane, Y., Ouchi, M., Oguri, M., et al. 2023, ApJS, 265, 5
Hellwing, W. A., Nusser, A., Feix, M., & Bilicki, M. 2017, MNRAS, 467, 2787
Hirano, S., & Yoshida, N. 2024, ApJ, 963, 2
Hoffman, Y., Courtois, H. M., & Tully, R. B. 2015, MNRAS, 449, 4494
Hoffman, Y., & Ribak, E. 1991, ApJL, 380, L5
Jenkins, a. R., Frenk, C. S., White, S. D. M., et al. 2001, MNRAS, 321, 372
Johnson, B. D., Leja, J., Conroy, C., & Speagle, J. S. 2021, ApJS, 254, 22
Katz, N., White, S. D. M., Katz, N., & White, S. D. M. 1993, ApJ, 412, 455
Kauffmann, G., White, S. D. M., & Guiderdoni, B. 1993, MNRAS, 264, 201
Kennicutt, R. C. 1998, ApJ, 498, 541
Kennicutt, R. C., & De Los Reyes, M. A. C. 2021, ApJ, 908, 61
Kennicutt, R. C., Evans, N. J., Kennicutt, R. C., & Evans, N. J. 2012, ARA&A, 50, 531
Krumholz, M. R., Burkhart, B., Forbes, J. C., & Crocker, R. M. 2018, MNRAS, 477, 2716
Larson, R. B. 1974, MNRAS, 169, 229
Lilow, R., Nusser, A., Lilow, R., & Nusser, A. 2021, MNRAS, 507, 1557
Ludlow, A. D., Borzyszkowski, M., & Porciani, C. 2014, MNRAS, 445, 4110
Ma, X., Hopkins, P. F., Garrison-Kimmel, S., et al. 2018, MNRAS, 478, 1694
Mason, C. A., Trenti, M., & Treu, T. 2015, ApJ, 813, 21
Mason, C. A., Trenti, M., & Treu, T. 2023, MNRAS, 521, 497
Mauerhofer, V., & Dayal, P. 2023, MNRAS, 526, 2196
Mitchell, P. D., Lacey, C. G., Lagos, C. D., et al. 2018, MNRAS, 474, 492
Mo, H. J., Mao, S., & White, S. D. M. 1998, MNRAS, 295, 319
Moster, B. P., Naab, T., & White, S. D. M. 2013, MNRAS, 428, 3121
Moster, B. P., Naab, T., & White, S. D. M. 2020, MNRAS, 499, 4748
Nadler, E. O., Benson, A., Driskell, T., Du, X., & Gluscevic, V. 2023, MNRAS, 521, 3201
Nusser, A., & Silk, J. 2022, MNRAS, 509, 2979
Okalidis, P., Grand, R. J. J., Yates, R. M., & Kauffmann, G. 2021, MNRAS, 504, 4400
Pacifici, C., Iyer, K. G., Mobasher, B., et al. 2023, ApJ, 944, 141
Padmanabhan, H., & Loeb, A. 2023, ApJL, 953, L4
Pallottini, A., & Ferrara, A. 2023, A&A, 677, L4
Parashari, P., & Laha, R. 2023, MNRASL, 526, L63
Peebles, P. J. E. 1980, Large-scale Structure of the Universe (Princeton, NJ: Princeton Univ. Press)
Pérez-González, P. G., Costantin, L., Langeroodi, D., et al. 2023, ApJL, 951, L1
Planck Collaboration, Aghanim, N., Akrami, Y., et al. 2020, A&A, 641, A6
Press, W. H., & Schechter, P. 1974, ApJ, 187, 425
Puchwein, E., & Springel, V. 2013, MNRAS, 428, 2966
Ren, K., Trenti, M., & Mason, C. A. 2019, ApJ, 878, 114
Riess, A. G., Anand, G. S., Yuan, W., et al. 2023, ApJL, 956, L18
Robertson, B. E., Kravtsov, A. V., Tinker, J., & Zentner, A. R. 2009, ApJ, 696, 636
Robertson, B. E., Tacchella, S., Johnson, B. D., et al. 2023, NatAs, 7, 611
Rodriguez-Puebla, A., Behroozi, P., Primack, J., et al. 2016, MNRAS, 462, 893
Rodríguez-Puebla, A., Primack, J. R., Avila-Reese, V., & Faber, S. M. 2017, MNRAS, 470, 651
Romano-Diaz, E., Faltenbacher, A., Jones, D., et al. 2005, ApJL, 637, L93
Sabti, N., Munoz, J. B., & Kamionkowski, M. 2024, PRL, 132, 061002
Schaller, M., Borrow, J., Draper, P. W., et al. 2024, MNRAS, 530, 2378
Schaller, M., Gonnet, P., Draper, P. W., et al., 2018 SWIFT: SPH With Interdependent Fine-grained Tasking, Astrophysics Source Code Library, ascl:1805.020
Schmidt, M. 1959, ApJ, 129, 243
Seppi, R., Comparat, J., Nandra, K., et al. 2021, A&A, 652, A155
Shen, X., Vogelsberger, M., Boylan-Kolchin, M., Tacchella, S., & Kannan, R. 2023, MNRAS, 525, 3254
Sheth, R. K., & Tormen, G. 1999, MNRAS, 308, 119
Shuntov, M., McCracken, H. J., Gavazzi, R., et al. 2022, A&A, 664, A61
Silk, J., Begelman, M. C., Norman, C., Nusser, A., & Wyse, R. F. G. 2024, ApJL, 961, L39
Silk, J., & Rees, M. J. 1998, A&A, 331, L1
Stefanon, M., Bouwens, R. J., Labbe, I., et al. 2021, ApJ, 922, 29
Sun, G., Faucher-Giguère, C. A., Hayward, C. C., et al. 2023b, ApJL, 955, L35
Sun, G., Faucher-Giguere, C. A., Hayward, C. C., & Shen, X. 2023a, MNRAS, 526, 2665
Sun, G., & Furlanetto, S. R. 2016, MNRAS, 460, 417
Tacchella, S., Eisenstein, D. J., Hainline, K., et al. 2023, ApJ, 952, 74
Tinker, J., Kravtsov, A. V., Klypin, A., et al. 2008, ApJ, 688, 709
Wang, B., Leja, J., Labbé, I., et al. 2023, ApJS, 270, 12
Wang, H., Mo, H. J., Yang, X., et al. 2016, ApJ, 831, 164
White, S. D. M., & Frenk, C. S. 1991, ApJ, 379, 52
Whitler, L., Stark, D. P., Endsley, R., et al. 2023, MNRAS, 519, 5859
Yang, H., Gao, L., Frenk, C. S., et al. 2023, MNRAS, 518, 5253
Yang, X., Mo, H. J., van den Bosch, F. C., Zhang, Y., & Han, J. 2012, ApJ, 752, 41
Yung, L. Y. A., Somerville, R. S., Finkelstein, S. L., Popping, G., & Dave, R. 2019, MNRAS, 483, 2983
Yung, L. Y. A., Somerville, R. S., Finkelstein, S. L., Wilkins, S. M., & Gardner, J. P. 2024, MNRAS, 527, 5929